Combustion, flow and spray dynamics for aerospace propulsion

Large-Eddy Simulation of combustion instabilities in a variable-length combustor

Simulation aux grandes échelles des instabilités de combustion dans un brûleur de longueur variable

Romain Garby [a,b,*], Laurent Selle [a,b], Thierry Poinsot [a,b]

[a] *Institut de Mécanique des Fluides, UMR CNRS/INP-UPS 5502, Allée du Professeur Camille Soula, 31400 Toulouse, France*
[b] *CNRS; IMFT; 31400 Toulouse, France*

A B S T R A C T

This article presents a simulation of a model rocket combustor with continuously variable acoustic properties thanks to a variable-length injector tube. Fully compressible Large-Eddy Simulations are conducted using the AVBP code. An original flame stabilization mechanism is uncovered where the recirculation of hot gases in the corner recirculation zone creates a triple flame structure. An unstable operating point is then chosen to investigate the mechanism of the instability. The simulations are compared to experimental results in terms of frequency and mode structure. Two-dimensional axi-symmetric computations are compared to full 3D simulations in order to assess the validity of the axi-symmetry assumption for the prediction of mean and unsteady features of this flow. Despite the inaccuracies inherent to the 2D description of a turbulent flow, for this configuration and the particular operating point investigated, the axi-symmetric simulation qualitatively reproduces some features of the instability.

© 2012 Académie des sciences. Published by Elsevier Masson SAS. All rights reserved.

R É S U M É

Cet article présente la simulation d'un injecteur expérimental de type moteur-fusée dont les propriétés acoustiques peuvent varier continûment grâce à un tube d'injection de longueur variable. Des simulations aux grandes échelles (LES) sont réalisées à l'aide du code AVBP. Un mécanisme de stabilisation de la flamme original montrant le rôle important de la recirculation de gaz chauds en entrée de chambre est observé. Un point de fonctionnement instable est ensuite choisi pour étudier le mécanisme de l'instabilité. Les simulations numériques sont comparées aux mesures du banc d'essai en termes de fréquence de l'instabilité et de structure du mode instable. Une simulation 2D axi-symétrique est comparée à une simulation 3D avec pour objectif de tester l'hypothèse de symétrie pour la prédiction de l'écoulement moyen et instationnaire de cette configuration. Bien que la description en 2D d'un coulement turbulent soit une simplification importante, pour cette configuration et dans le cas du point de fonctionnement choisi,

* Corresponding author at: Institut de Mécanique des Fluides, UMR CNRS/INP-UPS 5502, Allée du Professeur Camille Soula, 31400 Toulouse, France.
E-mail addresses: romain.garby@imft.fr (R. Garby), laurent.selle@imft.fr (L. Selle), thierry.poinsot@imft.fr (T. Poinsot).

le calcul axi-symétrique reproduit qualitativement certaines caractéristiques de l'instabilité.

1. Introduction

Most high-performance propulsion systems exhibit high-amplitude pressure oscillations at some stage in their design process. Unsteady heat release from combustion can couple with acoustic eigenmodes of the combustion chamber: this phenomenon is called combustion instability [1–3]. These instabilities can lead to important stresses and heat fluxes on the chamber walls and injectors, sometimes even resulting in the destruction of the engine [4,5]. Combustion instabilities are very difficult to predict because of the wide range of physical phenomena involved (acoustics, turbulence, chemical reactions, etc.) and they are often discovered at an advanced phase of the conception program.

A trial-and-error methodology with incremental modifications of the engine is usually necessary to recover stability but the associated cost is prohibitive. Therefore, the prediction of combustion instabilities through numerical simulation is a major issue. For gas turbine or aeronautic propellers, several studies have already been conducted [6–12] but for rocket engines the number of unsteady simulations is smaller [13–18]. This could be explained by the extreme thermodynamic conditions in rocket engines and the wide range of length scales: the characteristic length of the injector is a fraction of a millimeter while the flame length can be several dozens of centimeters.

In terms of numerical framework, the best way to study combustion instabilities and all the phenomena involved would be compressible Direct Numerical Simulation (DNS) with the full resolution of the Navier–Stokes equations. However, this method is inapplicable because of the prohibitive number of mesh points necessary to resolve the complex geometry and the high Reynolds-number flow of a rocket combustion chamber. Large-Eddy Simulation (LES) is a good candidate to study these instabilities and it has been used successfully in the field of gas turbines [19–22] for example to capture one mode of instability. What is more difficult to do is to predict transition from stable to unstable flow which is the ultimate objective in many practical cases: it is unclear today whether LES can predict stability limits. Moreover, the cost of full 3D LES for multiple operating points remains high. For geometries which are axi-symmetric, the question of performing only 2D axi-symmetric LES to explore stability maps much more rapidly becomes interesting. The objective of this paper is to explore this point with a model rocket engine by performing both 2D axi-symmetric and full 3D LES and comparing results to experimental data. The CVRC setup operated at Purdue University [23] is axi-symmetric and exhibits very strong unstable modes. This system works at high pressure and has a variable injector duct length which allows to explore stability limits in a continuous manner. The experimental setup and operating point are described in Section 2. The numerical method is then presented in Section 3 together with the computational domain and boundary conditions. Finally, the results of the numerical simulations are presented in Section 4.

2. Experimental setup

2.1. Description

The burner studied in this paper was designed and operated at Purdue University (Indiana, USA) [23–25]. The system is called Continuously Variable Resonance Chamber (CVRC) because the length of the oxidizer injector can be varied continuously, allowing for a detailed investigation of the coupling between the acoustics and combustion in the chamber. The CVRC, presented in Fig. 1, is an axi-symmetric burner with a 15-inch long (38.1 cm) combustion chamber closed by a choked nozzle. The reactants are fed into the chamber by a coaxial injector: oxidizer at the center and fuel at the periphery. For a continuous tuning of the acoustic response of the CVRC, the oxidizer-post length (L_{op}) can vary from $L_{op} = 3.5$ in. (8.89 cm) to $L_{op} = 7.5$ in. (19.05 cm), with respect to the inlet of the combustion chamber. The inlet of the oxidizer post is also choked so that the acoustic boundary conditions are well defined. Six pressure transducers are installed along the burner to measure high-frequency pressure fluctuations: the first one is located 3 in upstream of the injector face, and the remaining sensors are placed in the combustion chamber at 0.5, 1.5, 2.5, 3.5 and 14.5 in downstream of the injector face. These locations are respectively called P_1 to P_6 in the remainder of the paper.

2.2. Operating point

The fuel is pure gaseous methane injected at a rate of $\dot{m}_f = 0.0272$ kg s^{-1} and temperature $T_f = 300$ K. The oxidizer is a mixture of 90% hydrogen peroxide and 10% water (per mass unit), which is fully decomposed: this is equivalent to 42% oxygen and 58% water. The oxidizer is injected in the chamber at $T_{ox} = 1030$ K (both water and oxygen are in gaseous phase) and $\dot{m}_{ox} = 0.3180$ kg s^{-1}. Consequently, the global equivalence ratio is $\phi = 0.813$.

Accounting for all the species in the GRI-Mech 3.0 mechanism (52 species), the adiabatic burnt-gases temperature at equilibrium is $T_b^{ad} = 2512$ K. Since the total flow rate going through the choked nozzle is known ($\dot{m} = \dot{m}_{ox} + \dot{m}_{fuel} = 0.3452$ kg s^{-1}) assuming the chamber temperature, T_c, is equal to the adiabatic burnt-gases temperature at equilibrium T_b^{ad}, the chamber pressure P_c can be determined using:
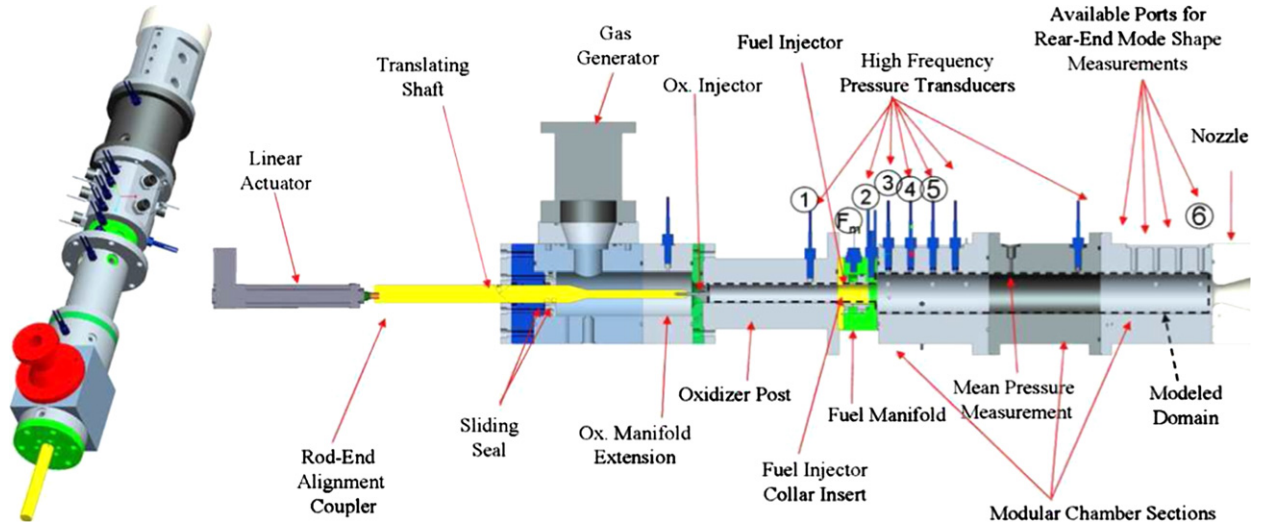
Fig. 1. Experimental setup installed at Purdue University: the CVRC [25]. Figure courtesy of Pr. W. Anderson, Purdue University.

Table 1
Operating point.

	Experiment	LES
Heat losses	Unknown	0
Combustion efficiency	Unknown	1
Chamber static temperature T_c	≈ 1904 K	2512 K
Chamber static pressure P_c	1.34 MPa	1.54 MPa

$$\dot{m} = \frac{c_d A P_0}{\sqrt{r T_0}} \gamma^{\frac{1}{2}} \left(\frac{2}{\gamma + 1} \right)^{\frac{\gamma+1}{2(\gamma-1)}} \tag{1}$$

The stagnation pressure and temperature, respectively P_0 and T_0 are given by:

$$P_0 = P_c \left(1 + \frac{\gamma - 1}{2} M^2 \right)^{\frac{\gamma}{\gamma-1}}; \qquad T_0 = T_c \left(1 + \frac{\gamma - 1}{2} M^2 \right) \tag{2}$$

where M is the Mach number of the burnt gases in the chamber, A the area of the choked nozzle, γ the ratio of heat capacities, r the perfect gas constant and c_d the discharge coefficient. Using $c_d = 1$, $T_c = T_b^{ad}$, $\gamma = 1.182$ and $r = 389.2$ (computed from the burnt-gases composition), one predicts a theoretical mean chamber pressure $P_c^{th} = 1.543$ MPa. The mean pressure actually measured in the experiment is $P_c^{xp} = 1.34$ MPa, which implies that heat losses or incomplete combustion lead to a lower burnt-gases temperature: $T_c < T_b^{ad}$. Using Eq. (1) backwards in order to obtain $P_c = P_c^{xp}$, yields $T_c^{xp} = 1904$ K. Because the simulations presented in Section 4 show that the combustion is complete (there is no unburnt fuel exiting the nozzle), this reduced temperature is attributed to thermal losses at the combustor walls. This approximate evaluation corresponds to a total heat loss at the walls equal to 25% of the available power (Table 3). Because the present work does not include heat losses, in the LES, the burnt-gases temperature is T_b^{ad} and the chamber pressure is 1.54 MPa (Table 1). The resulting increase in the speed of sound yields a small shift of the unstable mode frequency, as discussed in Section 4.3.

2.3. Stability

The experimental stability map (amplitude of pressure fluctuations versus L_{op}) is presented in Fig. 2 for a number of runs where the oxidizer-post is either translated forward (L_{op} increases), backward or kept constant during the whole test. Three different behaviors of the system can be distinguished:

  (i) **Stable** regions for $L_{op} < 3.75$ in (9.5 cm) and $L_{op} > 7.1$ in (18 cm).
 (ii) An **unstable** range for $3.75 < L_{op} < 6.3$ in (9.5 to 16 cm).
(iii) A zone of **hysteresis** for $6.3 < L_{op} < 7.1$ in (16 to 18 cm).

Because one the objectives of the present work is to compare 2D axi-symmetric and 3D computations to compute an unstable operating point, the simulations are conducted for $L_{op} = 4.75$ in (~ 12 cm). This value of L_{op} is also chosen to minimize potential hysteresis effects in the instability as all tests show strong pressure fluctuations under these conditions.
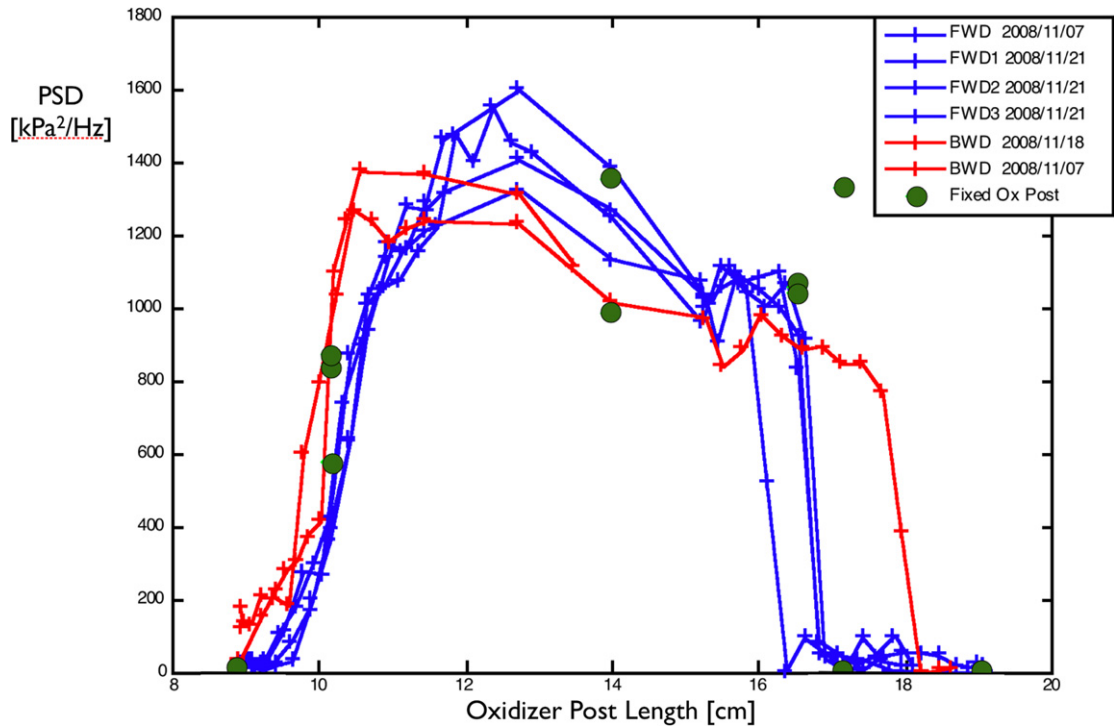
Fig. 2. Stability map of the CVRC combustor (experimental results [25]). Power spectral density of the pressure fluctuation at the frequency of the instability measured by probe P_2 ($x = 3.81$ cm). ———— : forward translation of the oxidizer post, ———— : backward translation and • : fixed oxidizer-post length. Figure courtesy of Pr. W. Anderson, Purdue University.

Table 2
Burnt-gases properties in thermodynamic conditions of the CVRC.

Eq. ratio	z	Scheme	T_b^{ad} [K]	Y_{CH_4}	Y_{O_2}	Y_{CO_2}	Y_{CO}	Y_{H_2O}	Y_{N_2}
1	$z_{st} = 0.095$	Gri-Mech	2661	$< 10^{-4}$	2.49×10^{-2}	2.22×10^{-1}	2.45×10^{-2}	7.12×10^{-1}	0
		2-step	2781	$< 10^{-4}$	2.25×10^{-2}	1.99×10^{-1}	3.94×10^{-2}	7.39×10^{-1}	0
0.813	$z_{xp} = 0.079$	Gri-Mech	2512	$< 10^{-4}$	7.50×10^{-2}	2.06×10^{-1}	6.17×10^{-3}	6.99×10^{-1}	0
		2-step	2586	$< 10^{-4}$	7.81×10^{-2}	2.02×10^{-1}	8.62×10^{-3}	7.11×10^{-1}	0

3. Numerical method

3.1. Solver and models

The simulations are carried out with the AVBP code developed at CERFACS [6,7,26] that solves the compressible Navier–Stokes equations on unstructured grids. The numerical scheme is the second-order in space and time Lax–Wendroff formulation [27]. Turbulence is modeled using the classical Smagorinsky model [28]. The flame/turbulence interaction is accounted for by the Dynamically Thickened Flame (DTF) model [29]. In this approach, the flame is artificially thickened to be resolved on the LES mesh and subgrid reaction rate is recovered through an efficiency function [30].

The CH_4/O_2 kinetics are modeled using a reduced two-step mechanism (BFER [31]) that accounts for six species (CH_4, O_2, CO_2, CO, H_2O and N_2) and two reactions:

$$CH_4 + \tfrac{3}{2}O_2 \longrightarrow CO + 2H_2O$$
$$CO + \tfrac{1}{2}O_2 \longleftrightarrow CO_2 \tag{3}$$

The first equation is irreversible while the second one is reversible and leads to an equilibrium between CO and CO_2 in the burnt gases. This scheme was developed for CH_4/air flame and used here without modification.

A common shortcoming of two-step mechanisms is that burning rates are over-predicted for rich mixtures. Following the procedure presented in [31], the present scheme uses a pre-exponential constant of the first reaction that is a function of the local equivalence ratio so as to recover accurate burning rates in rich mixtures. This scheme was validated for the thermodynamic conditions of the CVRC versus the Gri-Mech 3.0 mechanism. First, equilibrium states were compared to ensure that no important species would be neglected. Table 2 presents the burnt-gases properties for both schemes at
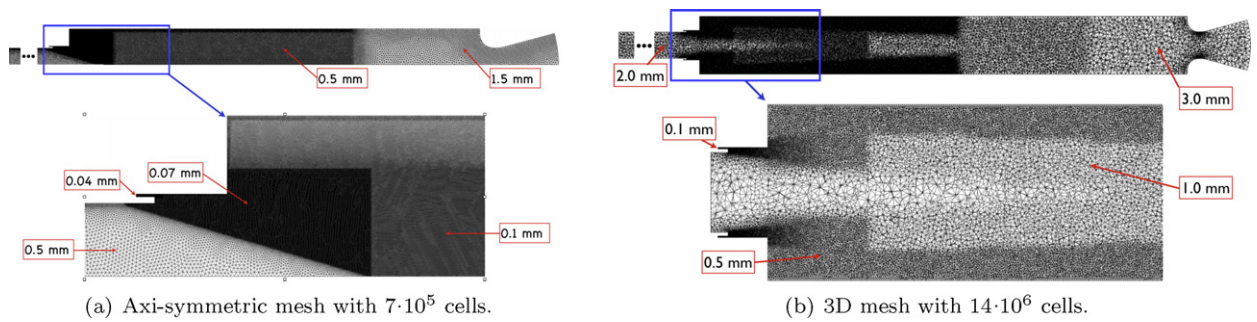
(a) Axi-symmetric mesh with $7 \cdot 10^5$ cells.

(b) 3D mesh with $14 \cdot 10^6$ cells.

Fig. 3. Detailed view of the two meshes.

the stoichiometric mixture fraction $z_{st} = 0.095$ as well as the average mixture fraction of the experimental operating point $z_{xp} = 0.079$ (calculated from the mass flow rates $\dot{m}_f$ and $\dot{m}_{ox}$). Even though it is expected that the combustion regime is a diffusion flame, the premixed laminar flame speeds at stoichiometry are compared: $s_L = 1.59$ m s^{-1} for Gri-Mech 3.0 and $s_L = 1.52$ m s^{-1} for the present two-step scheme. It was also checked that auto-ignition times for Gri-Mech like for the 2-step scheme are much larger than the residence time in the chamber. This is consistent with the fact that under the conditions of the CVRC experiment, combustion is not controlled by auto-ignition. Overall, these calculations validate the approximations implied by the use of the reduced scheme.

3.2. Computational domain and boundary conditions

With the advent of massively parallel computers and codes that scale on thousands of processors, three-dimensional (3D) simulations of turbulent combustion in complex geometries are now quite common in the research community. The AVBP solver is particularly attune for such computations [21,32,33]. However, because the background idea of the use of numerical simulations is to provide a quick and relatively inexpensive evaluation of the stability of a given configuration, we opted for a different approach: it was decided to compare the accuracy of a 3D computation using significant resources and a 'light' axi-symmetric computation feasible on lost-cost computer clusters. This study is performed for a single unstable operating point. The typical shortcoming of axi-symmetric computations is that turbulence being essentially a 3D phenomenon, the 2D assumption may yield incorrect vortex dynamics and the symmetry condition that imposes zero turbulent fluxes on the axis is inadequate. The consequences of these approximations will be addressed in Section 4.

Axi-symmetric computations were performed on a relatively fine mesh using 7×10^5 cells while three-dimensional computations use a mesh of 14×10^6 cells (Fig. 3). Because of the variety of length scales in the geometry (oxidizer tube diameter is 4 cm whereas fuel injector thickness is 0.4 mm) unstructured meshes are required. Cell sizes were chosen to ensure a correct resolution of the dynamic of the flow in the mixing zone and of the chemical and heat transfer of the flame downstream the injector. The computational time for 1 ms of physical time (that is more than one cycle of the instability) is 5 CPU hours on 32 processors of the SGI Altix ICE 8200 of CINES (Intel Quad-Core E5472) for the axi-symmetric mesh and 2 CPU hours on 512 processors of the same machine for the 3D mesh (6.4 times more expensive). The computational domain starts slightly downstream of the choked inlet of the oxidizer post and ends after the exit nozzle, which allows for well defined acoustic boundary conditions. Fuel is injected through an annular slit corresponding to the experiment but the tubes feeding the slit are not included. The boundary conditions are prescribed using the NSCBC technique [34]: mass flow rate and temperature are imposed at the oxidizer ($\dot{m}_{ox} = 0.32$ kg s^{-1} and $T_{ox} = 1030$ K) and fuel ($\dot{m}_f = 0.027$ kg s^{-1} and $T_f = 300$ K) inlets while nothing needs to be imposed at the supersonic outlet. Walls are treated as no-slip and adiabatic.

## 4. Results and discussion

This section is devoted to the comparison of the 2D axi-symmetric and 3D computations as well as the validation against available experimental data. Mean flow fields are compared in Section 4.1 and the flame-stabilization and dynamics are presented in Section 4.2. Finally Section 4.3 presents the analysis of the acoustic mode of this operating point in terms of structure and mechanism of the instability.

4.1. Mean flow field

Once a permanent regime has been reached in both computations, the flow is averaged to compute the mean properties. For both simulations, the averaging time is 18 ms, which corresponds to more than 25 cycles of the instability (*cf.* Section 4.3) and about 10 flow-through times of the chamber. The axial velocity field is presented in Fig. 4 where the upper and lower parts show respectively the 2D and 3D simulation. The black iso-contour is the zero axial velocity, which highlights the recirculation zones. The flow fields are quite different: first, the axi-symmetric simulation presents a longer corner-recirculation zone but it also maintains a larger axial velocity close to the axis. These differences are not due to the
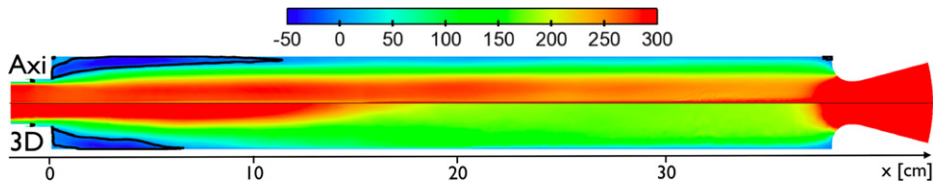
Fig. 4. Average field of axial velocity in a longitudinal cut of the CVRC with $u = 0$ iso-line highlighting the recirculation zones. *Top*: 2D axi-symmetric, *bottom*: 3D.
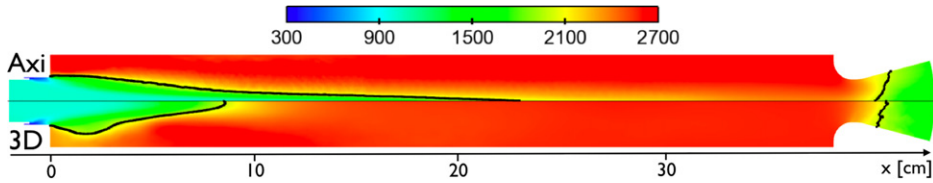
Fig. 5. Average temperature field with $T = 2000$ K iso-line to highlight the mean position of the turbulent flame brush. *Top*: 2D axi-symmetric, *bottom*: 3D.
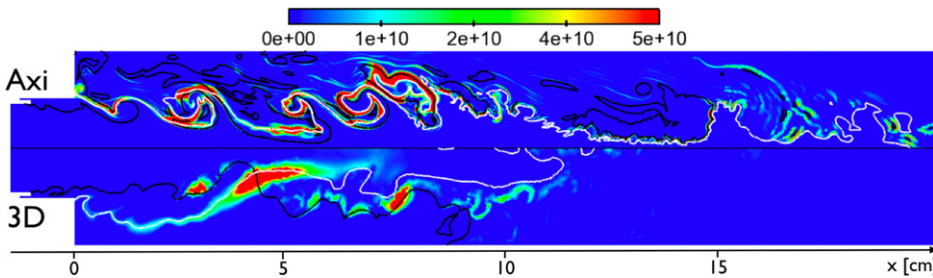
Fig. 6. Instantaneous field of heat release rate (W m^{-3}). *Black iso-line*: stoichiometric mixture fraction ($z = z_{st}$); *white iso-line*: temperature $T = 2000$ K. *Top*: 2D axi-symmetric, *bottom*: 3D.

grid resolution as a significant effort was done to resolve the recirculation zones (Fig. 3). Even though the no-slip boundary is clearly a rough condition that could be replaced by an adequate wall-law model, the 3D simulation with larger cells at the wall does a better job in the second half of the chamber. The mean temperature field is plotted in Fig. 5 together with a black iso-contour at $T = 2000$ K in order to represent the mean position of the turbulent flame brush. There is a striking difference between the two simulations as the flame length is over-estimated by a factor of three in the 2D computation. This feature is typical of axi-symmetric computations where the boundary condition on the axis imposes zero turbulent fluctuations. The flapping movement of the flame on the axis is impossible resulting in a longer average flame. This elongated flame could be the origin of the distorted axial velocity field. The 3D computation also has a lower mean temperature in the corner recirculation zones that is attributed to a wider flapping motion of the flame (*cf.* Section 4.2).

4.2. Flame stabilization and dynamics

For the analysis of the stabilization of the flame in the combustion chamber, an instantaneous longitudinal cut of the heat-release rate is presented in Fig. 6. Two iso-lines are superimposed: temperature $T = 2000$ K (in white) as a delimitation between fresh and burnt gases and mixture fraction $z = z_{st}$ (in black) to highlight the regions where the fuel and oxidizer are in stoichiometric proportions. In both simulations, the stoichiometric iso-line (black lines) starts at the fuel injector and continues into the chamber while the temperature iso-line (white lines) is anchored at the junction between the chamber and the injector. Both fields are distorted by turbulent structures but the convolution is more intense in the 2D case, which is typical of such simulations where the dynamics of the vorticity is massively affected by the 2D assumption. As inferred from the mean fields (Fig. 5), the lack of turbulent fluctuations on the axis of the 2D computation affects the dynamics of the flame front resulting in a much longer flame. In the 2D case, the mixture fraction and temperature iso-contours are much closer but the structure of the reaction layer is similar in both computations: most of the reaction rate is sitting on the temperature iso-contour and extremely intense heat release rate occurs where the two contours cross. This peculiar flame structure can be seen as a special triple flame [35], produced by a triple layer: fuel, oxidizer and burnt gases (Fig. 7(b)). It shows that chemistry is not sufficiently fast in the CVRC to stabilize the flame at the lips where fuel is injected. Stabilization is produced by the burnt gases recirculating at the dump plane. Fig. 7 illustrates the mechanism suggested by these results: oxidizer and fuel start mixing at the lips where methane is injected; no combustion exists in this zone. Downstream, this mixture is heated by the recirculating hot gases and the flame reaches a maximum intensity when the high temperature line crosses the stoichiometric line, creating a structure very similar to the BGS (Burnt Gas
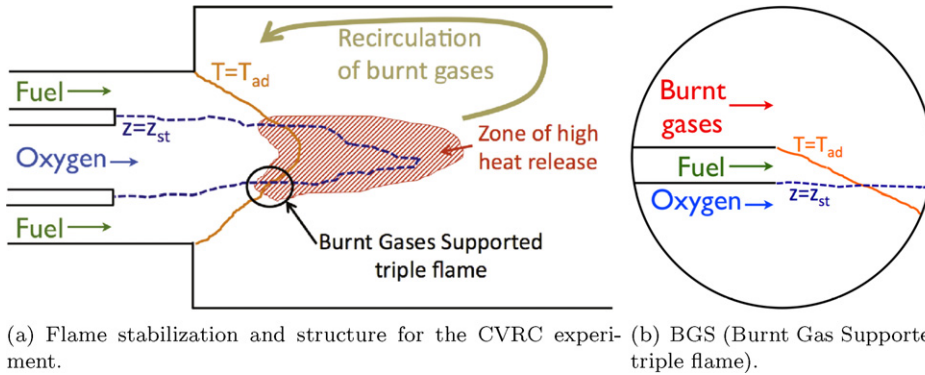
(a) Flame stabilization and structure for the CVRC experiment.

(b) BGS (Burnt Gas Supported triple flame).

Fig. 7. Schematic representation of the flame stabilization and structure for the CVRC experiment and a BGS triple flame.

(a) Temporal evolution of $P_{ad} = (P - \overline{P})/\overline{P}$ at P2. $RMS(ax) = 0.06$, $RMS(3d) = 0.11$.

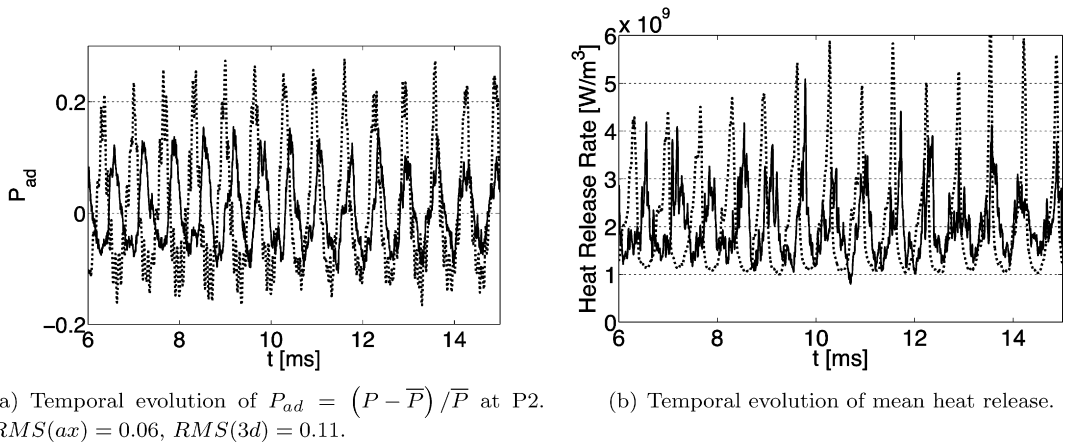(b) Temporal evolution of mean heat release.

Fig. 8. - - - 3D, —— axi-symmetric.

Supported) triple flame computed by Jiménez and Cuenot [36]. This observation also explains why a very high resolution is required to predict flame stabilization here: the mixing zone between fuel and oxidizer must be properly meshed but the whole chamber must also be well resolved to capture the recirculation zones which are controlling the stabilization.

4.3. Analysis of the unstable acoustic mode

The experimental investigation of the operating point $L_{op} = 4.75$ in shows that a strong unstable acoustic mode occurs at a frequency $F^{xp} = 1400$ Hz with an amplitude (power spectral density at the frequency of the instability measured at probe P_2) between 1200 and 1500 kPa^2 Hz^{-1}. We will now test the ability of the numerical simulations to recover these characteristics. The temporal evolution of the pressure signal at probe P$_2$ is plotted in Fig. 8(a). The signal seems mildly non-linear and high-frequency harmonics are visible on top of the main unstable mode. The frequency of the fundamental is $F^{2D} = 1572$ Hz for the 2D axi-symmetric computation and $F^{3D} = 1510$ Hz for the 3D case. The discrepancy between the simulations and the experiment ($F^{xp} \approx 1400$ Hz) is caused by the different values of the mean pressure, resulting in a slight shift of the speed of sound. In terms of amplitude, the root mean square (rms) of the 3D signal is twice as much as that of the 2D computation. This difference will be explained later in this section with the analysis of the acoustic energy equation. Then the space-averaged heat release rate versus time is presented in Fig. 8(b). Unlike the pressure signal, the heat release response is non-linear, which is to be expected for finite amplitude combustion instabilities. The harmonic content of the 2D simulation is wider than that of the 3D case, which may be related to the overall higher small-scale wrinkling of the flame surface shown in Fig. 6. The spatial structure of the unstable mode (Fig. 9) was obtained by performing a power spectral density analysis of the whole field at the frequency of the instability. The longitudinal variation of the modulus and phase of the pressure fluctuations are plotted in Figs. 9(a) and 9(b), respectively. It appears that in the combustion chamber ($x > 0$), the instability has a half-wave mode shape, while in the oxidizer tube, the pressure fluctuations are mainly propagative. Both simulations predict nearly identical structures, with a minor deviation in the modulus around the junction between the injector and the chamber.
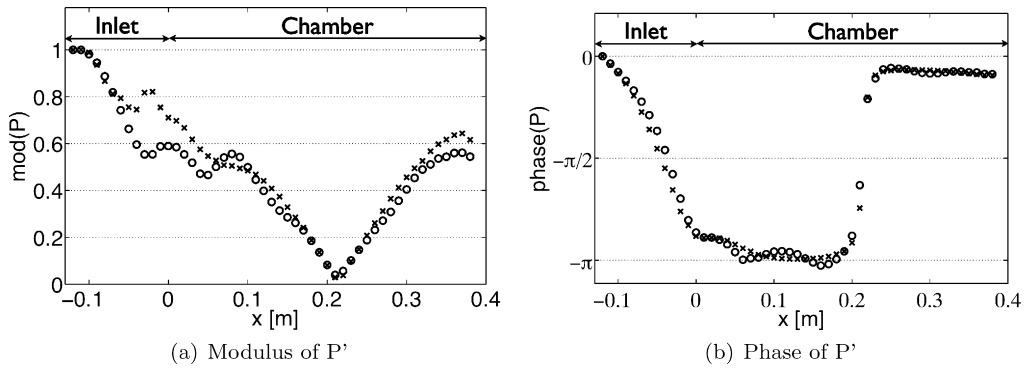
(a) Modulus of P'

(b) Phase of P'

Fig. 9. Structure of the acoustic field, ×: 3D, ○: 2D axi-symmetric.

Table 3
Time-averaged value of the Rayleigh source term, *R*, of acoustic energy and burner power output, P_b, for both simulations.

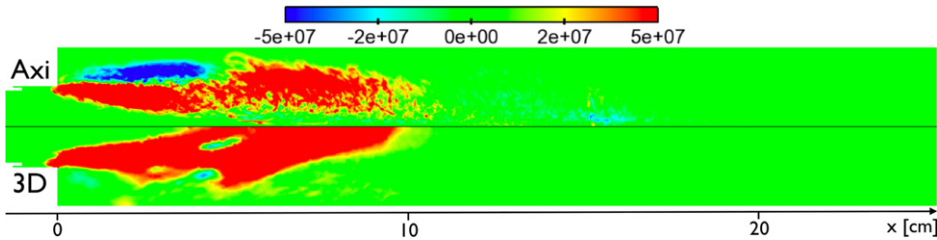| Simulation	R [W]	P_b [W]
2D axi	$3.08 \cdot 10^3$	$1.37 \cdot 10^6$
3D	$8.23 \cdot 10^3$	$1.34 \cdot 10^6$

Fig. 10. Time-averaged field of local Rayleigh term, *r*. *Top*: 2D axi-symmetric, *bottom*: 3D.

The mean acoustic energy E_a over a cycle of the instability is defined as:

$$E_a = \frac{1}{\tau} \int_t^{t+\tau} \int_V \frac{1}{2}\left(\overline{\rho}u'^2 + \frac{p'^2}{\overline{\rho}c^2}\right) dv \, dt \tag{4}$$

where u', p', and ρ are respectively the acoustic velocity, the pressure fluctuation and the mean density, *c* is the speed of sound and τ is the period of one unstable cycle. A conservation equation for the acoustic energy may then be derived [20,37]:

$$\frac{\partial E_a}{\partial t} = R - F \tag{5}$$

where the Rayleigh source term, *R*, and the flux of acoustic energy through the boundaries, *F*, are defined by:

$$R = \frac{1}{\tau} \int_t^{t+\tau} \int_V \frac{\gamma - 1}{\gamma \overline{p}} p'\dot{\omega}' \, dv \, dt \quad \text{and} \quad F = \frac{1}{\tau} \int_t^{t+\tau} \int_\Sigma p'\mathbf{u}'.\mathbf{n} \, d\sigma \, dt \tag{6}$$

where *V* is the volume of the domain and Σ its boundary; $\dot{\omega}'$ is the fluctuation of heat release rate and **n** the outward normal of Σ.

The source term of acoustic energy due to the unsteady combustion, *R*, is then compared to the mean power output, P_b, of the burner. The values reported in Table 3 indicate that the Rayleigh term is much larger in the 3D case, as expected from the amplitude of the pressure fluctuations presented in Fig. 8(a).

The value of the global Rayleigh term, *R*, is a measure of the overall contribution of the flame to the acoustic energy. In order to assess the impact of the various portions of the flame, a local time-averaged Rayleigh term, *r*, is defined as:

$$r = \frac{1}{\tau} \int_t^{t+\tau} \frac{\gamma - 1}{\gamma \overline{p}} p'\dot{\omega}' \, dt \tag{7}$$

A longitudinal cut of r through the combustion chamber of the CVRC is presented in Fig. 10. Despite being similar in size and shape, there are two major differences between the 2D and 3D simulations. First, in the 3D case, the Rayleigh term is overwhelmingly positive while a significant zone of negative r is observed in the recirculation zone of the 2D computation. Then, on the axis of the 2D computation, the lack of turbulent fluctuations drives r toward zero, which is not the case in 3D. Finally, it seems that the longer tail of the flame seen in 2D (for $x > 10$ cm) does not contribute significantly to the acoustic energy. This may explain why in term of prediction of the instability, the 2D computation yields results similar to the 3D case.

5. Conclusion

An unstable operating point of a model rocket combustor with continuously variable acoustic properties is simulated using both low-cost 2D axi-symmetric and detailed 3D calculations. The axi-symmetric simulation does not predict the correct mean properties of the flow (velocity, the flame length, etc.) or the flapping movement of the flame due to the boundary condition on the axis that imposes zero turbulent fluctuations. An unusual structure of the stabilization flame is observed: the flame looks like a distorted triple flame with a strong rich premixed branch and a weak diffusion tail, stabilized by the recirculation of burnt gases at the entrance of the combustion chamber. Nevertheless, both simulations exhibit a combustion instability with virtually identical frequency and structure of the acoustic mode. The frequency of the instability compares favorably with the experimental data. The contribution of the flame to acoustic energy is larger for the 3D geometry than for the 2D one, resulting in a larger amplitude of the pressure fluctuation (7.4 bars instead of 4.7 bars). Despite the differences in the flow field, for this configuration and this operating point, the 2D axi-symmetric simulation qualitatively reproduces some features of the instability.

Acknowledgement

References

[1] P. Clavin, E.D. Siggia, Turbulent premixed flames and sound generation, Combust. Sci. Technol. 78 (1991) 147–155.
[2] D.J. Harrje, F.H. Reardon, Liquid propellant rocket instability, Technical Report SP-194, NASA, 1972.
[3] F.E.C. Culick, P. Kuentzmann, Unsteady Motions in Combustion Chambers for Propulsion Systems, NATO Research and Technology Organization, 2006.
[4] G. Searby, D. Rochwerger, A parametric acoustic instability in premixed flames, J. Fluid Mech. 231 (1991) 529–543.
[5] S. Candel, D. Durox, T. Schuller, Flame interactions as a source of noise and combustion instabilities, in: 10th AIAA/CEAS Aeroacoustics Conference – AIAA 2004-2928, 2004.
[6] L. Selle, G. Lartigue, T. Poinsot, R. Koch, K.-U. Schildmacher, W. Krebs, B. Prade, P. Kaufmann, D. Veynante, Compressible large-eddy simulation of turbulent combustion in complex geometry on unstructured meshes, Combust. Flame 137 (4) (2004) 489–505.
[7] S. Roux, G. Lartigue, T. Poinsot, U. Meier, C. Bérat, Studies of mean and unsteady flow in a swirled combustor using experiments, acoustic analysis and large eddy simulations, Combust. Flame 141 (2005) 40–54.
[8] T.C. Lieuwen, V. Yang, F.K. Lu, Combustion Instabilities in Gas Turbine Engines: Operational Experience, Fundamental Mechanisms and Modeling, American Institute of Aeronautics and Astronautics, 2005.
[9] Danning You, Ying Huang, Vigor Yang, A generalized model of acoustic response of turbulent premixed flame and its application to gas-turbine combustion instability analysis, Combust. Sci. Technol. 117 (2005) 1109–1150.
[10] H. Pitsch, Large eddy simulation of turbulent combustion, Annu. Rev. Fluid Mech. 38 (2006) 453–482.
[11] K.-U. Schildmacher, A. Hoffman, L. Selle, R. Koch, C. Schulz, H.-J. Bauer, T. Poinsot, Unsteady flame and flow field interaction of a premixed model gas turbine burner, Proc. Combust. Inst. 31 (2007) 3197–3205.
[12] N. Noiray, M. Bothien, B. Schuermans, Investigation of azimuthal staging concepts in annular gas turbines, Combust. Theory Model. 15 (5) (2011) 585–606.
[13] Suresh Menon, Wen-Huei Jou, Large-eddy simulations of combustion instability in an axisymmetric ramjet combustor, Combust. Sci. Technol. 75 (1–3) (1991) 53–72.
[14] Sankaran Venkateswaran, Jeffrey Grenda, Charles L. Merkle, Computational fluid dynamic analysis of liquid rocket combustion instability, in: 10th AIAA Computational Fluid Dynamics Conference, Honolulu, HI, June 1991.
[15] J.C. Oefelein, V. Yang, Modeling high-pressure mixing and combustion processes in liquid rocket engines, J. Prop. Power 14 (5) (1998) 843–857.
[16] J.C. Oefelein, Mixing and combustion of cryogenic oxygen–hydrogen shear-coaxial jet flames at supercritical pressure, Combust. Sci. Technol. 178 (1–3) (2006) 229–252.
[17] Nan Zong, Vigor Yang, Cryogenic fluid jets and mixing layers in transcritical and supercritical environments, Combust. Sci. Technol. 178 (2006) 1–3.
[18] T. Schmitt, Y. Méry, M. Boileau, S. Candel, Large-Eddy Simulation of oxygen/methane flames under transcritical conditions, Proc. Combust. Inst. 33 (1) (2011) 1383–1390.
[19] P. Schmitt, T. Poinsot, B. Schuermans, K.P. Geigle, Large-eddy simulation and experimental study of heat transfer, nitric oxide emissions and combustion instability in a swirled turbulent high-pressure burner, J. Fluid Mech. 570 (2007) 17–46.
[20] T. Poinsot, D. Veynante, Theoretical and Numerical Combustion, third edition, www.cerfacs.fr/elearning, 2011.
[21] G. Staffelbach, L.Y.M. Gicquel, G. Boudier, T. Poinsot, Large eddy simulation of self-excited azimuthal modes in annular combustors, Proc. Combust. Inst. 32 (2009) 2909–2916.
[22] C. Fureby, LES of a multi-burner annular gas turbine combustor, Flow Turbul. Combust. 84 (2010) 543–564.
[23] Y.C. Yu, L.A. O'Hara, J.C. Sisco, W.E. Anderson, Experimental study of high-frequency combustion instability in a continuously variable resonance combustor, in: 47th AIAA Aerospace Sciences Meeting, Orlando, Florida, January 2009.

[24] J.C. Sisco, Y.C. Yu, V. Sankaran, W.E. Anderson, Examination of mode shapes in an unstable model combustor, J. Sound Vib. 330 (1) (2011) 61–74.
[25] Y. Yu, J.C. Sisco, S. Rosen, A. Maghav, W.E. Anderson, Spontaneous longitudinal combustion instability in a continuously-variable resonance combustor, J. Prop. Power 28 (5) (2012) 876–887.
[26] V. Moureau, G. Lartigue, Y. Sommerer, C. Angelberger, O. Colin, T. Poinsot, Numerical methods for unsteady compressible multi-component reacting flows on fixed and moving grids, J. Comput. Phys. 202 (2) (2005) 710–736.
[27] P.D. Lax, B. Wendroff, Systems of conservation laws, Comm. Pure Appl. Math. 13 (1960) 217–237.
[28] J. Smagorinsky, General circulation experiments with the primitive equations: 1. The basic experiment, Mon. Weather Rev. 91 (1963) 99–164.
[29] J.-Ph. Légier, T. Poinsot, D. Veynante, Dynamically thickened flame LES model for premixed and non-premixed turbulent combustion, in: Proc. of the Summer Program, Center for Turbulence Research, NASA Ames/Stanford Univ., 2000, pp. 157–168.
[30] F. Charlette, D. Veynante, C. Meneveau, A power-law wrinkling model for LES of premixed turbulent combustion: Part I – Non-dynamic formulation and initial tests, Combust. Flame 131 (2002) 159–180.
[31] B. Franzelli, E. Riber, M. Sanjosé, T. Poinsot, A two-step chemical scheme for Large-Eddy Simulation of kerosene–air flames, Combust. Flame 157 (7) (2010) 1364–1373.
[32] G. Staffelbach, T. Poinsot, High performance computing for combustion applications, in: Super Computing 2006, Tampa, Florida, USA, 2006.
[33] M. Boileau, G. Staffelbach, B. Cuenot, T. Poinsot, C. Bérat, LES of an ignition sequence in a gas turbine engine, Combust. Flame 154 (1–2) (2008) 2–22.
[34] T. Poinsot, S. Lele, Boundary conditions for direct simulations of compressible viscous flows, J. Comput. Phys. 101 (1) (1992) 104–129.
[35] P.N. Kioni, K.N.C. Bray, D.A. Greenhalgh, B. Rogg, Experimental and numerical study of a triple flame, Combust. Flame 116 (1998) 192–206.
[36] C. Jimenez, B. Cuenot, DNS study of stabilisation of turbulent triple flames by hot gases, Proc. Combust. Inst. 31 (1) (2007) 1649–1656.
[37] F. Nicoud, T. Poinsot, Thermoacoustic instabilities: should the Rayleigh criterion be extended to include entropy changes? Combust. Flame 142 (2005) 153–159.